



# Alloys-by-design: A low-modulus titanium alloy for additively manufactured biomedical implants

E. Alabort<sup>a</sup>, Y.T. Tang<sup>b</sup>, D. Barba<sup>b,d</sup>, R.C. Reed<sup>b,c,\*</sup>

<sup>a</sup> Allied Ltd., Unit 15, Oxford Industrial Park, Yarnton OX5 1QU, United Kingdom

<sup>b</sup> Department of Materials, University of Oxford, Parks Road, Oxford OX1 6HT, United Kingdom

<sup>c</sup> Department of Engineering Science, University of Oxford, Parks Road, Oxford OX1 3PJ, United Kingdom

<sup>d</sup> Escuela Técnica Superior de Ingeniería Aeronáutica y del Espacio, Universidad Politécnica de Madrid, Plaza Cardenal Cisneros, 3, Madrid 28040, Spain

## ARTICLE INFO

### Article history:

Received 26 November 2020

Revised 8 February 2022

Accepted 9 February 2022

Available online 18 February 2022

### Keywords:

Biomedical

Titanium alloys

Selective laser melting

Characterisation

Alloys-by-design

Low modulus

Additive manufacturing

## ABSTRACT

The performance of many metal biomedical implants – such as fusion cages for spines – is inherently limited by the mismatch of mechanical properties between the metal and the biological bone tissue it promotes. Here, an alloy design approach is used to isolate titanium alloy compositions for biocompatibility which exhibit a modulus of elasticity lower than the Ti-6Al-4V grade commonly employed for this application. Due to the interest in alloys for personalised medicine, additive manufacturability is also considered: compositions with low cracking susceptibility and with propensity for non-planar growth are identified. An optimal alloy composition is selected for selective laser melting, and its processability and mechanical properties tested. Additive manufacturing is used to engineer a heterogeneous microstructure with outstanding combined strength and ductility. Our results confirm the suitability of novel titanium alloys for lowering the stiffness towards that needed whilst being additively manufacturable and strong.

© 2022 The Authors. Published by Elsevier Ltd on behalf of Acta Materialia Inc.

This is an open access article under the CC BY-NC-ND license

(<http://creativecommons.org/licenses/by-nc-nd/4.0/>)

## 1. Introduction

Alloys for biomedical implants require performance characteristics which are multifunctional: trading off mechanical behaviour, biocompatibility and adequate manufacturability to tight tolerances [1–3]. Of overarching importance is mechanical compatibility with human bone, which is vital for successful integration with the body [4–6]. Stiffness mismatching between metal and bone causes stress shielding [7–10], which weakens the adjoining bone tissue and increases the risk of bone resorption, loosening, and implant rejection – see Fig. 1(a). At the cellular level, stiff materials can also affect the differentiation of cells into osteoblasts – the type of cell responsible for the formation of new bone. It has been shown that mechanical strain regulates and increases osteoblast proliferation and their subsequent transformation into osteocytes [11,12] – see Fig. 1(b). The evidence indicates that low modulus materials increase the speed and effectiveness of bone regeneration around metallic implants.

But the elastic moduli of bone and metals differ greatly. Human spongy bone ranges from 0.02 to 5 GPa [13,14], whilst for cortical bone – the harder more dense variant found in the periphery – values range from 10 to 40 GPa [13,14]. These values are substantially lower than those of most biomedical alloys: commercially pure titanium and Ti-6Al-4V (110–130 GPa), Co-Cr alloys (190–210 GPa), and 316L stainless steel (210–250 GPa) [15,16]. These may be impairing true implant compatibility and osseointegration [17,18]. Although titanium and its alloys have good corrosion resistance [19,20] and bio-compatibility [21], concerns exist around the cytotoxicity of the alloying elements V and Al [22,23]. There is evidence that  $\beta$ -titanium alloys alloyed with so-called *vital* elements (Nb,Ta,Mo,Zr) exhibit lower cytotoxicity and improved cell viability when compared to Ti-6Al-4V [24,25]. Thus, there is a technological drive to design bio-compatible alloys – that do not contain toxic or hazardous metals such as V, Al, Co, Ni, and Cr – which have mechanical properties closer to human bone.

How best to process such new alloys? Additive manufacturing (AM) is becoming a pivotal technology for the fabrication of medical implants [26] with unique osseointegrative properties [27] and complex geometries that are impossible to produce using other processing methods [6,28,29]. For example, AM allows

\* Corresponding author at: Department of Engineering Science, University of Oxford, Parks Road, Oxford OX1 3PJ, United Kingdom.

E-mail address: [roger.reed@eng.ox.ac.uk](mailto:roger.reed@eng.ox.ac.uk) (R.C. Reed).

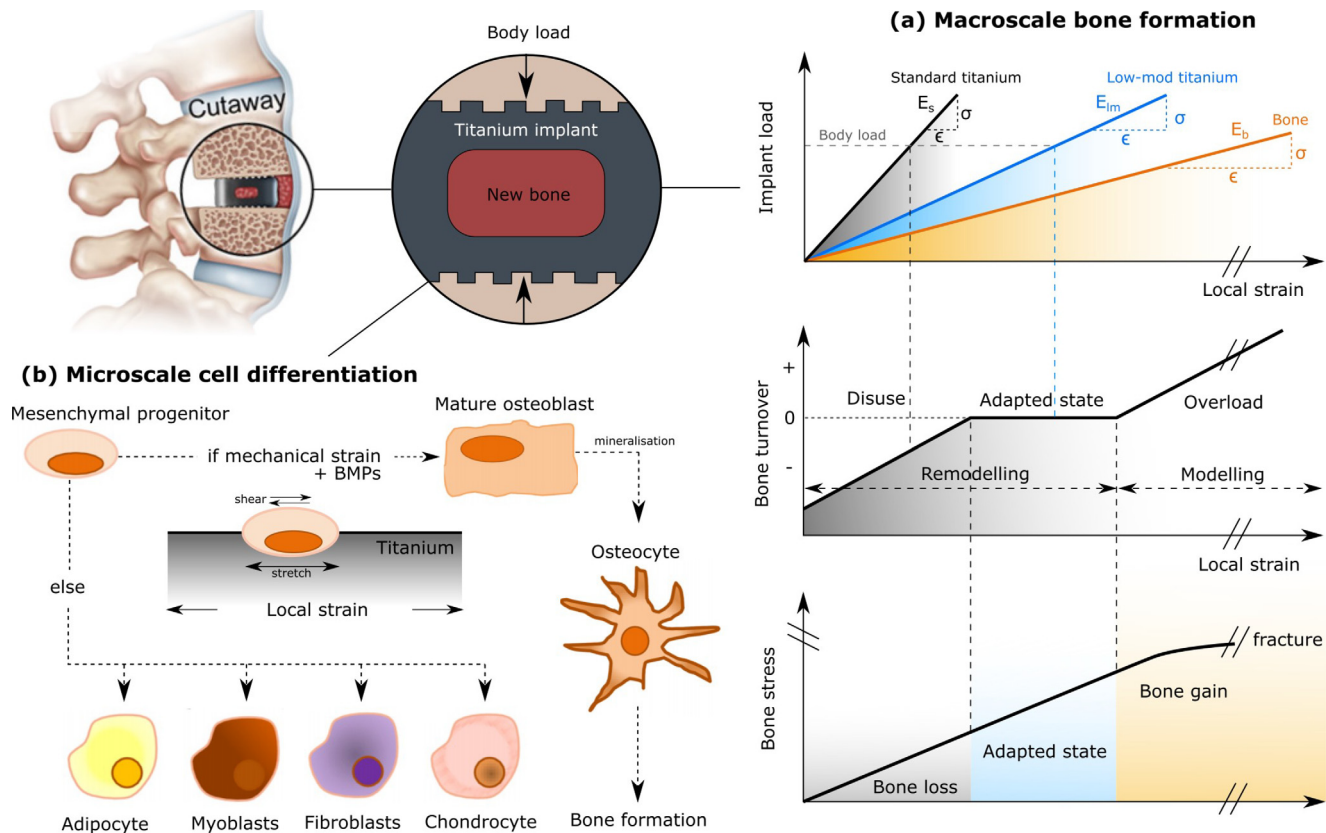


**Fig. 1.** Diagram showing the effect of implant material stiffness in: (a) bone formation at the macro scale, and (b) cell differentiation and osteocyte formation at the micro-scale.

for the manufacturing of custom implants that conform to medical imaging and thus are personalised for each patient [30,31]. Moreover, AM can produce architected porous structures into which bone can grow [32,33]. However, building complex structures require the alloys to be the most amenable to the additive process [34]: i.e. less likely to form defects such as cracks and pores [35] and more likely to build quality strut network for lattice structures [36]. For example, Ti-6Al-4V – the most used titanium alloy for biomedical applications – is known to grow via planar solidification during the additive process [37]. This characteristic creates large elongated microstructures that introduce scatter in properties, anisotropy, and low ductility. Alloys with a high growth restriction factor are more likely to circumvent this planar solidification behaviour, thus creating more optimal microstructures – see Fig. 2 – and overcoming these limitations.

The research reported in this paper has been carried out to address holistically the requirements of an alloy designed with the necessary attributes for this application: improved biocompatibility, reduced stiffness, good strength, and optimal additive manufacturability. First, an alloy design framework based on a merit index approach is used; this identifies clearly the trade offs which arise from the multifunctional nature of the problem [38,39]. This computational framework is then used to isolate optimal alloy chemistries; compositional optimisation is presented in detail in the supplementary material. Second, a promising new alloy is chosen and manufactured in atomised powder form in order to be processable by powder bed selective laser melting methods. Third, the manufacturability is assessed via single-track, cube, and tensile builds – these are used to isolate optimal processing parameters. Fourth, three particular laser conditions are chosen and studied – the aim is to explain the observed mechanical differences from the microstructure. Finally, optimal parameters are used to

build tensile specimens which reveal the mechanical advantages of the new alloy over the conventional Ti-6Al-4V.

## 2. Experimental methods

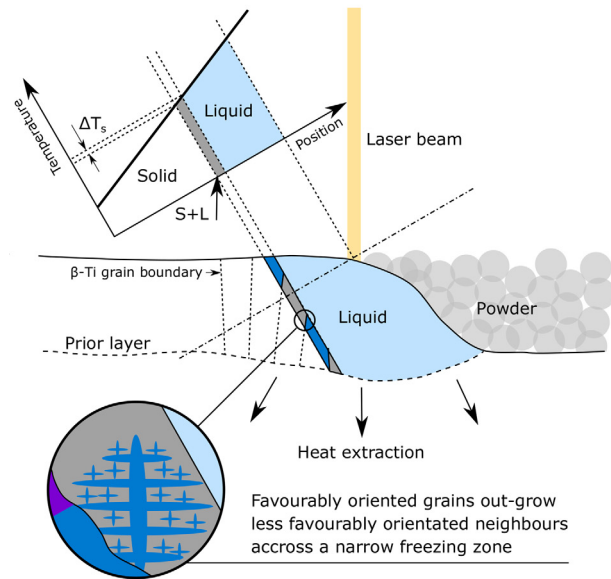
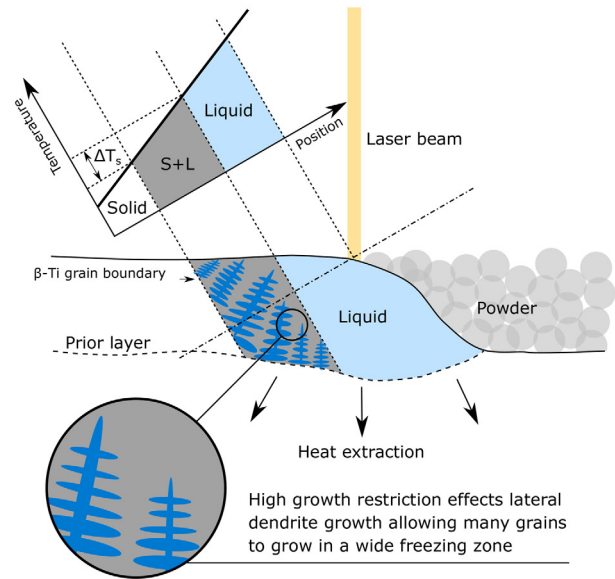
In this section, the method used to produce the alloy powder is explained, together with a description of the additive manufacturing process. Then, the experimental method employed to measure the mechanical properties is detailed.

### 2.1. Alloy production

The designed composition was produced in powder form following the electrode induction-melting gas atomization (EIGA) method. Before atomisation, the material was pre-alloyed in ingot form – this ensures homogeneous chemistry of the powder. After atomisation the powder was sieved to a range suitable for the selective laser melting process – i.e. a powder size distribution between 10 and 63  $\mu\text{m}$ . Fig. 3 shows a micrograph of the powder that was produced together with the measured distribution of particle sizes – one can see that the powder particles are spherical and relatively free of satellites – this will help with powder flowability. The chemistry of the alloy in powder form was analysed by inductively coupled plasma – optical emission spectrometry (ICP-OES) method.

### 2.2. Selective laser melting

Selective laser melting was carried out in a Renishaw AM400 machine using the reduced build volume chamber.

**(a) Narrow solidification - Low growth restriction (Ti6Al4V)****(b) Wide solidification - High growth restriction (Low-mod alloy)**

**Fig. 2.** Diagram illustrating different solidification behaviour between alloys with: (a) narrow solidification window and low growth restriction factor, and (b) wide solidification window and high growth restriction.

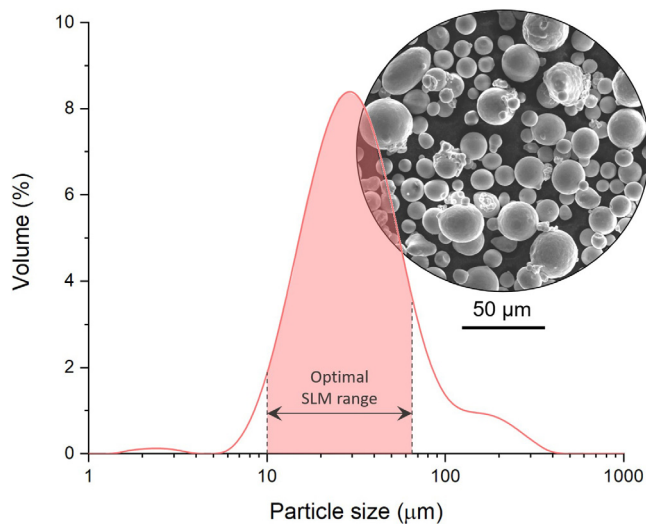


**Fig. 3.** Micrograph of the titanium powder used in this study together with the measured powder size distribution.

### 2.2.1. Deriving optimal parameters via single-tracks

First, a single-track design of experiment was carried out to isolate optimal laser parameters and to understand the relationship between energy input and melt-pool size. Different laser parameters were used to build 250 different  $10 \times 2$  mm fins. The laser power was ranged between 75 and 350 W, while varying the point distance and the scan speeds to achieve different combinations of energy densities. Then, the fins were analysed to isolate parameters that provided a stable melt pool and to relate the thickness of the fin to the input energy. For this purpose, the input enthalpy was used. This is defined following [40]

$$\Delta H = \frac{AP}{\rho \sqrt{\pi} D u \phi^3} \quad (1)$$

where  $A$  is absorptivity (assumed to be 0.65),  $P$  is the laser power,  $\rho$  is the density ( $6.07 \text{ g/cm}^3$ ),  $D$  is the thermal diffusivity (assumed to be  $1 \times 10^{-9}$ ),  $u$  is the laser speed, and  $\phi$  is the spot size.

### 2.2.2. Deriving optimal parameters via density cubes

Second, melt-stability is not enough to derive optimal parameters. One needs to make sure that when hatched, the melt tracks produce solid bulks absent of porosity and defects. For this purpose, a cube density build was carried out. The cubes measured  $4 \times 4 \times 4$  mm. After manufacturing, the cubes were mounted and polished. Optical microscopy was then used to quantify defects and porosity. The same build was carried out in Ti-6Al-4V to compare the processing window of the 2 alloys.

### 2.2.3. Deriving optimal parameters via tensile samples

Third, to understand the effect of laser parameters on tensile properties a net-shape tensile build was proposed. The influence of a wide variety of processing conditions on mechanical properties (i.e. elastic modulus, yield strength, and ductility) was studied using vertical net-shape tensile samples. 40 different combinations of laser parameters were employed. Different exposure times at laser powers of 100, 200, 300, and 400 W were studied. We employed three different hatch distances: 60, 90, and 120  $\mu\text{m}$ , and a variety of exposure times – all samples were build using a 30  $\mu\text{m}$  layer thickness. A comprehensive list of the employed material parameters is provided in the Appendix.

### 2.2.4. Understanding the role of microstructure on tensile behaviour

Machined tensile builds were used to isolate the effect of SLM surfaces on the mechanical properties and to understand the effect of microstructure with processing. For this purpose, we printed large solid blocks to extract bulk tensile samples. Solid blocks were manufactured both in vertical and horizontal orientations using 3 different sets of laser parameters – these summarised in the Appendix. In order to compare mechanical properties with current orthopaedic materials, a block of Ti-6Al-4V alloy was also manufactured. This was printed using the following parameters: 200 W laser power, 56  $\mu\text{m}$  of hatch distance, 70  $\mu\text{m}$  spot size, 30  $\mu\text{m}$  layer thickness, and 45  $\mu\text{s}$  exposure time. Samples measuring 40 mm in length, 3 mm in width and 1 mm in thickness with reduced gauge length measuring  $8 \times 1.5 \times 1 \text{ mm}^3$  were machined using electro discharge machining from the additive blocks. The samples were then plane polished to remove any damage from the surfaces. A second set of low-modulus alloy bulk tensile bars were stress re-

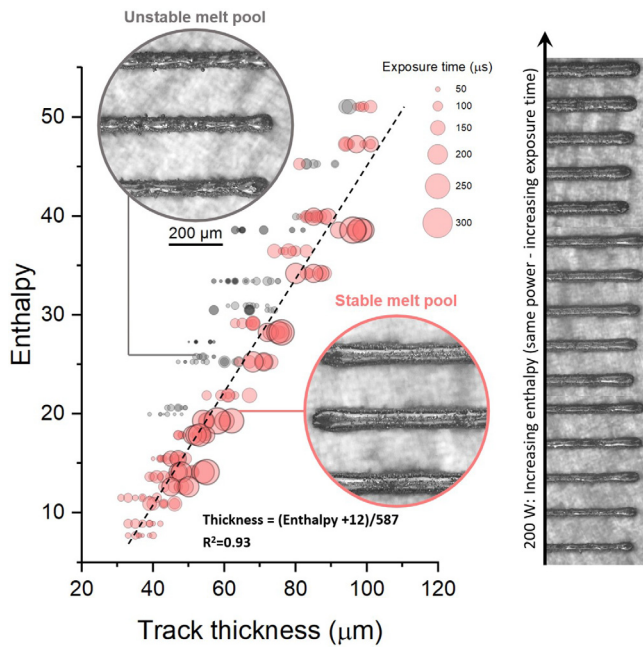


**Fig. 4.** Optical micrographs show an example of how the melt-pool changes with varying laser parameters. Detailed images show the difference between stable and unstable single-tracks. Graph shows the relationship between the single-track thickness and the enthalpy of the laser parameters.

lied at 750 °C for 1 h in an argon flooded furnace – the samples were machined from the centre of the bars, thus any oxidation and/or alpha-case present in the test samples is unlikely. This will allow us to compare the mechanical properties between the as-built and the stress-relieved conditions. In the case of Ti-6Al-4V, bulk tensile bars were stress relieved at 800 °C for 4 h in an vacuum furnace.

Mechanical testing of the samples was performed in a electro-mechanical Instron testing machine. Two sets of uniaxial tensile tests were performed: (1) constant strain rate until failure and (2) loading-unloading-reloading (LUR) tests (just for 100 W and 300 W vertical samples). All tests were carried out at a general strain rate of 0.001/s controlled by a contact extensometer. 2D strains during the test were monitored using digital imaging correlation techniques. Unloading points in LUR tests were selected every 3.5% strain approximately to extract the back stress at each processing condition. Back-stresses for each unloading-reloading curve were calculated following Yang et al. [41].

### 2.3. Scanning electron microscopy

Metallography samples were prepared using standard metallography procedures with the final step of colloidal silica suspension for five minutes. The characterisation was completed using a Zeiss Merlin field emission gun scanning electron microscope (FEG-SEM). Each sample was mounted in two orientations with surfaces denoted as XY- and XZ-planes, which were perpendicular and parallel as opposed to the build direction respectively. The beam was operated under a 15 kV acceleration voltage with a current density of 15 nA. A BRUKER electron backscatter diffraction (EBSD) detector was used to collect the diffraction patterns at a step size of 2.3 μm. The ESPIRIT 2.1 software was utilised for post-processing and grain size measurements, which is quoted as equivalent diameters.

Chemical analysis was carried out in the same SEM system with an Oxford Instrument X-MAX energy dispersive X-ray (EDX) spectroscopy detector. Samples after stress relieve treatment were

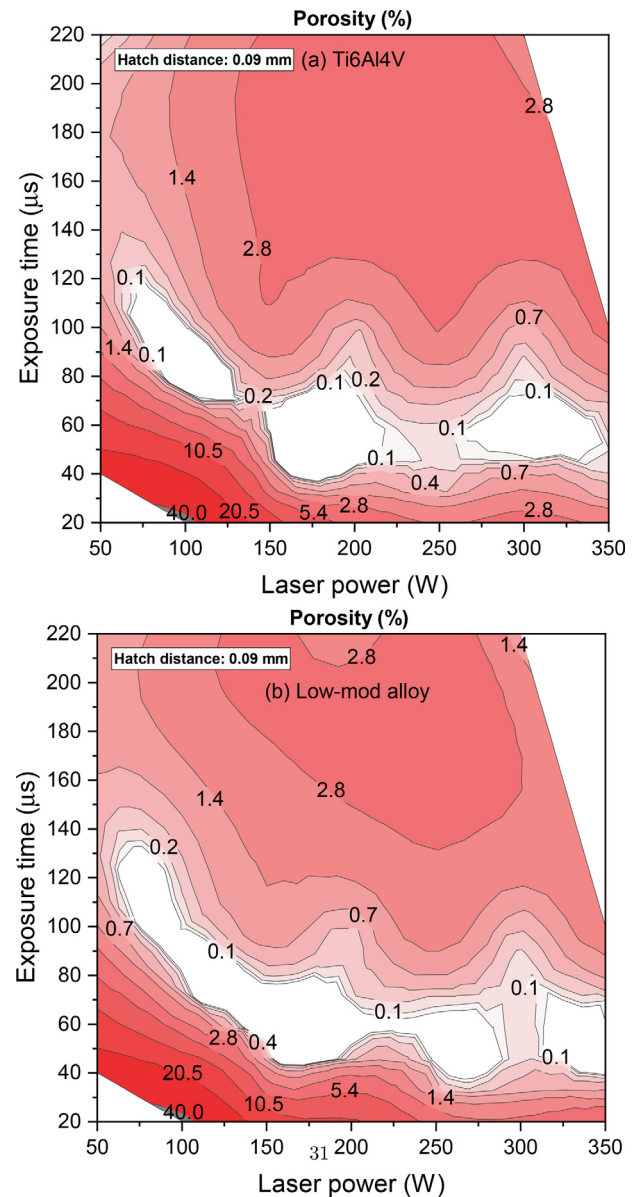


**Fig. 5.** Contour plots for the experimental area fraction of porosity (in %) as a function of exposure time and laser power for: (a) Ti6Al4V, and (b) novel low-mod alloy.

probed by line-analysis, at the step size of 0.03 μm, to detect the chemical enrichment of the intergranular phase.

Fractography were also conducted to examine the fracture behaviour between as-built and stress relieved microstructures. Moreover, to investigate the internal cavitation and cracking in association with deformation mechanism. Cross-sections parallel to the build direction (XZ-plane) was also captured using both secondary electron (SE) and backscattered electron (BSE) detectors.

## 3. Results and discussion

In this section we present and discuss the relationship between processing, microstructure, and mechanical properties.

### 3.1. On the optimisation of the processing conditions for the bio-β alloy

Optimising processing parameters is key to obtain fully dense parts but also to extract the most of the mechanical properties

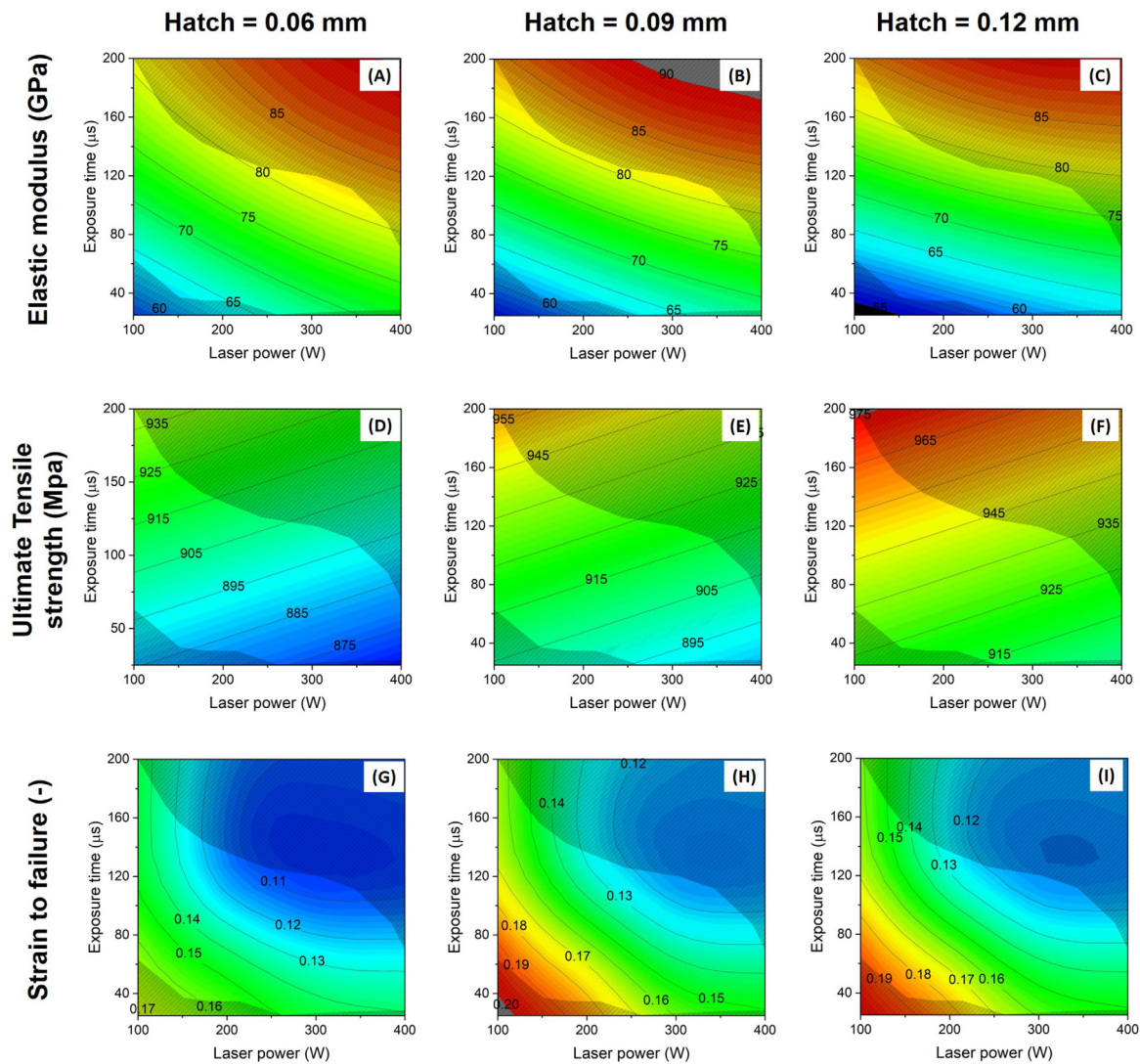


**Fig. 6.** Contour plots for the measured values of elastic modulus (a–c), ultimate tensile strength (d–f), and strain-to-failure (g–i) as a function of exposure time and laser power for: 0.06 mm (a, d & g), 0.09 (b, e & h), and 0.12 mm hatch distance (c, f & i).

that the alloy has to offer. This subsection presents a framework to carry out such optimisation.

### 3.1.1. Processing optimisation for stable melt-pools

Single-tracks are used to isolate combinations of laser parameters that give stable melt-pools. The laser power was ranged from 75 to 300 W with varying scan speeds (or exposure times). Then, optical microscopy was employed to determine whether the track was uniform or not – thus identifying stability. A uniform track of molten metal is considered stable while a track that is irregular with observable balling and irregular drops is considered unstable – Fig. 4 illustrates examples of both. An optical microscope was also used to measure the thickness of the track, thus relating the laser parameters and energy input to the width of the melt pool. The stability analysis of each track, their thickness, exposure time and enthalpy are plotted in Fig. 4. A linear regression between the melt-pool width and the enthalpy was found.

In Fig. 4 one can see that enthalpy itself cannot rationalise the observed melt-pool stability – stable tracks were found at every enthalpy level. However, there is certain correlation between the exposure time and the stability: when the exposure time is very small (small scatter data points) the pool is unstable independent of the power input. When the exposure time is large, the melt

pools are stable, but the thickness of the tracks increases substantially. A combination of high laser power and large exposure times may seem promising but further consideration must be given. The high energy associated can cause keyhole porosity, higher residual stresses, vaporisation, and excess of spatter [42]. Thus, thin stable melt-pools are desirable.

Isolating parameters that give stable and thin melt-pools is not enough. One needs to ensure that the material is in fully dense conditions when those track lines are next to each other forming solid bulk (hatching). For this purpose, a solid cube design-of-experiment with multiple processing parameters is presented next.

### 3.1.2. Effect of laser parameters on bulk density

Fig. 5 shows a contour plot of the measured porosity of the cubes for both Ti-6Al-4V (a), and the  $\beta$  low-mod alloy (b) as a function of laser power (x axis) and exposure time (y axis) using a fixed hatch distance (0.09 mm). The graph shows that both have a similar processing window (in terms of defects) at which the material achieves fully dense conditions. The results indicate that the low-mod alloy needs slightly higher energy densities to reach low porosity values – as evidenced by low-mod having slightly larger porosity under fast exposure times. Nevertheless, it is evident that there is a wide processing window in which one can operate. The

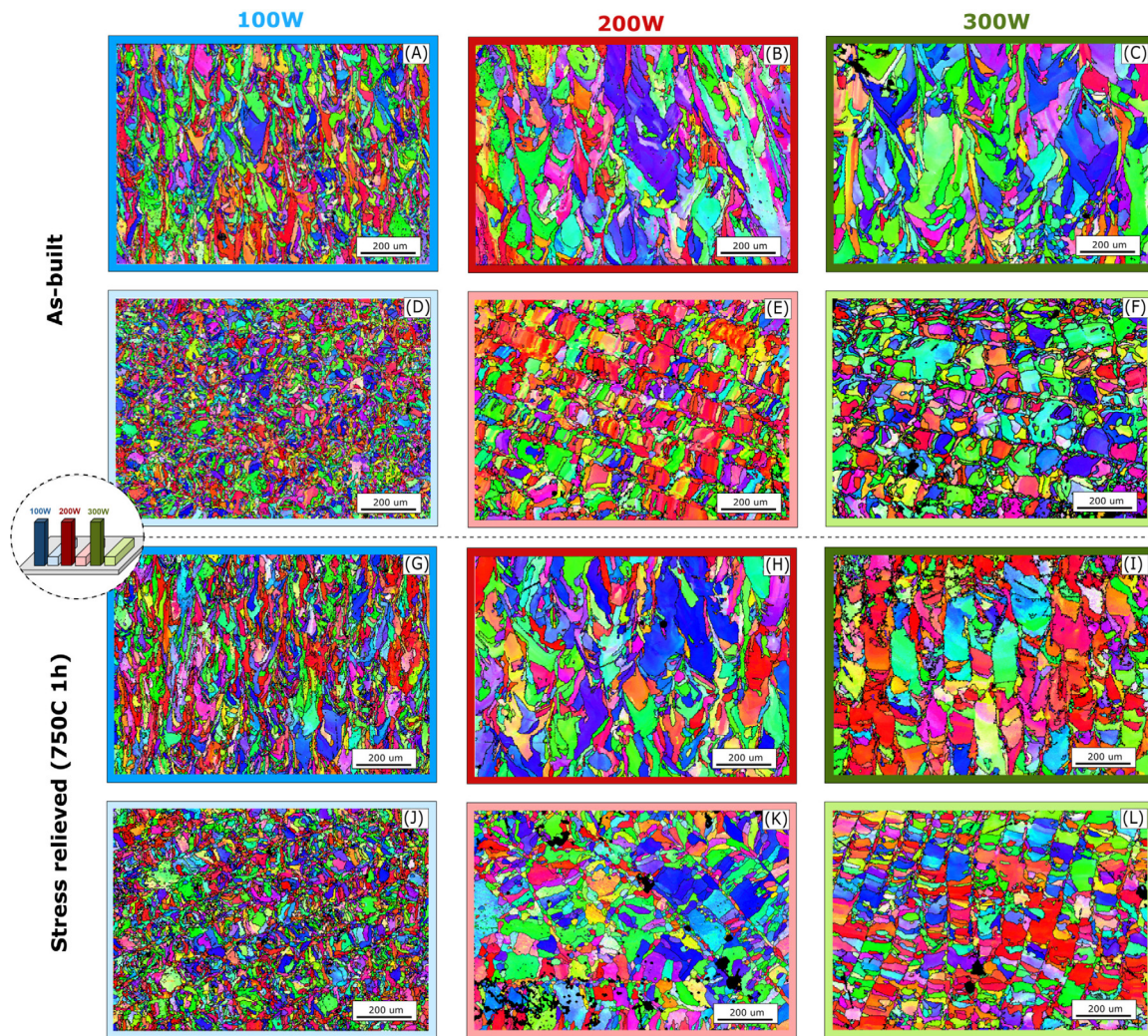


**Fig. 7.** EBSD maps of microstructures characterised in three different laser parameters. (a–f): IPF-X scans of the as-built microstructure processed using 100–300 W conditions in two orientations. (g–l): IPF-X scans of the stress-relieved microstructure processed using 100–300 W conditions in two orientations.

next section will focus on understanding how mechanical properties may vary within that operating window.

### 3.1.3. Effect of laser parameters on tensile properties

In this section, a mechanical analysis has been carried out to identify and understand the effect of processing conditions on the mechanical properties of the  $\beta$ -Ti alloys. For this purpose, tensile tests on net-shape samples with a wide range of different combinations of laser settings have been performed to identify optimal parameters.

The resulting mechanical curves of the  $\beta$ -Ti alloy as a function of the laser parameters are presented in the Appendix – we then extracted the critical property values (i.e. elastic modulus, ultimate tensile strength, and strain-to-failure). An automated regression model (Gaussian process regression built-in MATLAB's machine learning toolbox) with five-fold cross-validation to avoid over-fitting was then employed to extract relationships between processing conditions (laser power, exposure time, and hatch distance as inputs) and mechanical properties (elastic modulus, tensile strength, and ductility as outputs). The results of this exercise is contour plotted in Fig. 6. The shaded areas of Fig. 6 indicate conditions where porosity is expected to be higher than 0.2 % based on the results from Fig. 5 – thus areas where the model extrapolation may be invalid. One can see a strong dependency between

**Table 1**

Summary of the influence of the processing parameters on the mechanical properties of the  $\beta$ -Ti alloy

Parameter/Property	Elastic modulus	Strength	Ductility
Hatch distance ( $\uparrow$ )	$\downarrow$	$\uparrow$	$\uparrow$
Laser Power ( $\uparrow$ )	$\uparrow$	$\downarrow$	$\downarrow$
Exposure Time ( $\uparrow$ )	$\uparrow$	$\uparrow$	$\downarrow$

the laser settings – exposure time, laser power, and hatch distance – on the three metrics of interest. The elastic modulus increases as the hatching distance is reduced and the laser power and exposure time increased. Conversely, the ductility of the alloy is improved as the hatching distance is increased and the laser power and the exposure time decreased. Finally, for increasing the strength of the alloy, hatch distance and exposure time should be increased and laser power decreased. These relationships between processing parameters and mechanical properties of the alloy are summarised in Table 1.

Based on the diagrams in Fig. 6, a hatch distance of 0.12 mm gives a better balance of strength and stiffness than 0.06 and 0.09 mm. For a fixed hatching distance, different combinations of exposure times and laser powers might be selected to tailor the

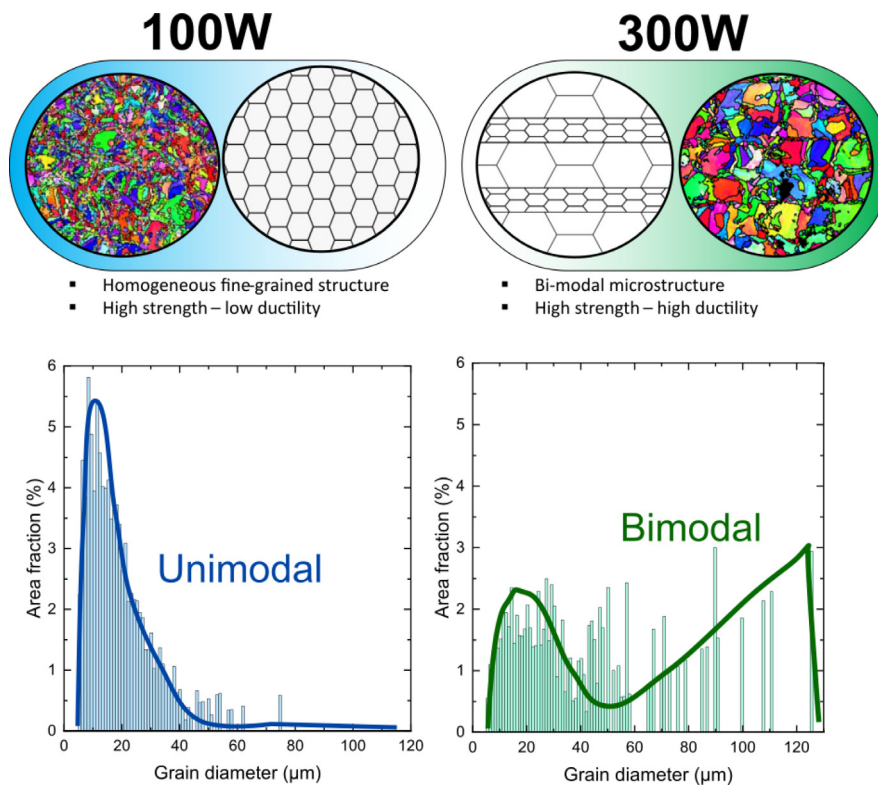


Fig. 8. Grain size distribution for 100 W, and 300 W indicating a transfer from an unimodal distribution (100 W) to a bimodal distribution (300 W).

strength and elastic modulus of the alloy based on the mechanical requirements.

### 3.2. Microstructure engineering for a high-strength ductile $\beta$ -Ti alloy

Processing conditions in additive manufacturing can affect substantially the mechanical properties of the new alloy. In this section, the change of properties by processing conditions is connected with the underlying changes in the microstructure. To this end, material with different power laser conditions (100, 200, and 300 W) was employed. More details of the laser strategies is given in Table A.7. First, the effect of the laser parameters on the microstructure is studied by means of EBSD statistical analysis. Then, the mechanical properties for the different laser conditions is measured and the connection with the microstructure is rationalised. Finally, the extracted insights from this analysis are then used to propose a superior microstructure for optimal combination of ductility and strength when compared with legacy alloys (e.g., Ti-6Al-4V).

#### 3.2.1. Effect of the processing conditions on the grain structure

Inverse pole figure maps of the microstructures obtained in the as-built (top) and stress-relieved (bottom) conditions are presented in Fig. 7. The material manufactured under each laser power demonstrates very different grain sizes and growth orientations. The grain size processed under the 100 W condition remained the smallest (42  $\mu\text{m}$ ), which it then increases with input laser power to 92 & 105  $\mu\text{m}$  for 200 W and 300 W respectively. This is in accordance with previous studies on other alloy systems [43]. On the other hand, Fig. 7 shows that the stress-relieved heat treatment has not caused a drastic change in grain size or grain distribution. Further analysis of the effect of the stress-relief heat treatment on the microstructure is presented in Section 3.3.

It is also noted that the grain structures at the 200 and 300 W conditions present a pronounced sandwich structure with alternate

layers of fine grains and coarse grains. This aspect is further confirmed by the grain size distribution analysis presented in Fig. 8. 300 W grain structure demonstrates a bimodal distribution in contrast to 100 W which has a unimodal distribution. This kind of bimodal structure has been observed in other alloys fabricated by additive manufacturing [44] and is associated with the laser path produced by the solidification conditions at high energy densities. These laser conditions contain a few oversized grains, which indicates its local properties may experience some degree of scattering.

Next, the effect of these microstructural changes on the mechanical properties is addressed.

#### 3.2.2. On the connection between processing conditions, mechanical properties and underlying microstructure

Samples were machined out from 100, 200 and 300 W additively manufactured blocks to isolate any surface effect on mechanical properties. Samples were tested both in vertical and horizontal directions to the build plate. Mechanical responses as a function of the power conditions are reported in the Appendix for both in as-built (top) and stress relieved conditions (bottom). These curves are processed and the mechanical properties – i.e., ductility, yield strength and stiffness – are presented in Fig. 9. Based on this data, the mechanical properties of the  $\beta$ -Ti alloy are found highly dependent upon build direction and processing conditions. Lower power (100 W) shows higher strength and stiffness with lower ductility while high power (300 W) exhibit higher elongations to failure and lower elastic moduli at expense of a decrease of strength. Medium power values (200 W) present high values of stiffness and moderate strength while achieving large fracture strains comparable to ductile 300 W material. Stress relieved material exhibits a drastic drop in performance: a higher elastic moduli and lower ductility is observed without any improvement of the strength. A significant ductility reduction is captured in all stress-relieved microstructures regardless to laser parameters employed. This event is particularly pronounced in the materials processed in

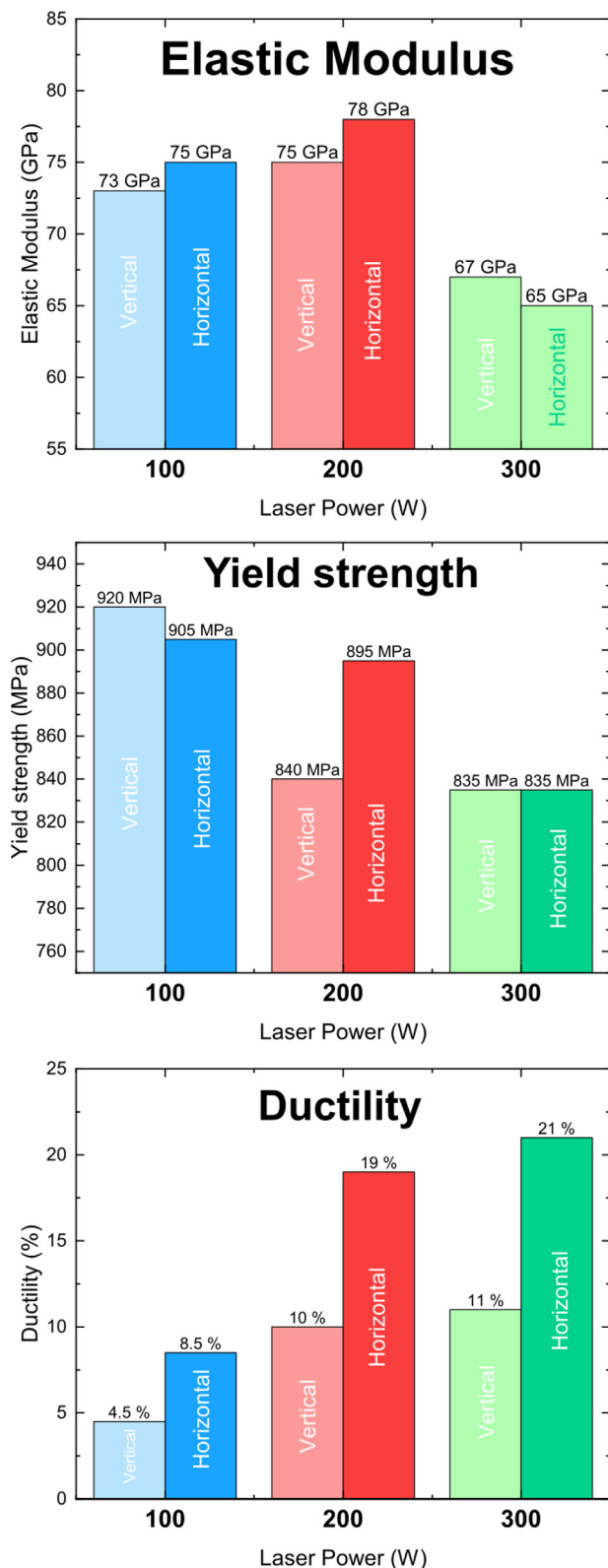


**Fig. 9.** Influence of the laser power on the elastic modulus (top), yield strength (middle) and ductility (bottom) of additively manufactured  $\beta$ -Ti alloy. Data extracted from Fig. 10.

the 300 W conditions. This drop of mechanical properties associated with the stress-relief process is rationalised in Section 3.3 by understanding how laser parameters and heat treatment change the underlying microstructure of the bulk material.

The extraordinary increase in ductility observed between low power modes (100 W) and medium-high power modes (200–300 W) needs further rationalisation. The strain-hardening rate ( $\Theta = \frac{\partial \sigma}{\partial \epsilon}$ ) of 100 W and 300 W samples has been extracted from the stress-strain curves and presented in Fig. 10 for horizontal and vertical directions. The necking points for each sample identified from the DIC sequence is indicated by red marks. A necking point of 134% and 214% is found for horizontal and vertical directions, respectively. Furthermore, a continuously high level of strain-hardening is associated with delay of necking phenomena during the plastic deformation of metals and consequently an increase of ductility [45–47]. Therefore an increase of the hardening rate is desirable for a ductile behaviour. In Fig. 10, for both directions, the strain-hardening rate of the bimodal structure (300 W) demonstrates a sudden drop after the yielding point associated with the yield peak in Fig. 10 and then a strong recovery of  $\Theta$  above the level of the unimodal microstructure (100 W) producing a delay in the necking.

That increase of the strain hardening capability of the 300 W samples might be a result of the bimodal sandwich microstructure observed in Fig. 8 and will be discussed next. In the 100 W, a small grain structure demonstrates a high critical stress for plastic deformation. This is due to the Hall-Petch effect in which grain boundaries act as barriers for dislocation motion, thus having small grains reduced free paths for dislocation motion and increased critical stress for dislocation gliding. This produces a rapid accumulation of dislocations at the grain boundaries once the gliding stress is reached. This rapid accumulation of dislocations produces a strong strain hardening which adds to the high yielding stress led to the fracture stress of the material at low strains. On the other hand, for the 300 W bimodal microstructure the evolution of the plastic process is schematised in Fig. 11. First, the large grain bands start deforming as the critical stress is reached due to its soft nature rationalised by the hall effect. This led to a lower yield stress than for the fine unimodal 100 W microstructure in accordance with Fig. 9. This is the region defines as soft-slip in which most of the plastic deformation is absorbed by the large low-yield stress grains. This strain partitioning produce an accumulation of dislocations at the grain boundaries of the large grains. This is known to produce the presence of long-range back stress [48] and thus strain-hardening. The restriction of the small grains to deform produce gradually more geometrically necessary dislocations (GND), increasing the back stress thus maintaining the level hardening rate and retarding the localised necking of the plastic deformation. This is known as 'hard-wrap' slip. Fracture can occur in any point of the sample, when the fracture stress is reached. This process has been previously observed in other alloy systems (Fe, Ti) with bimodal microstructures [46,47]. To confirm the presence of this hardening mechanism, back stress measurements have been performed by means of loading-unloading-reloading (LUR) tests on the 100 W and 300 W samples. The results are presented in Fig. 12. The measured back-stress is considerably higher for the bimodal 300 W microstructure and demonstrates a continuous increase as the strain increases in accordance with the previous assumptions. In contrast, 100 W unimodal microstructure shows lower values of back stress and reduced increase rate in accordance with a lower number of GNDs due to the more homogeneous deformation of the microstructure when compared to the bimodal case. In our opinion, the rationalisation of the improvement of the ductility in this alloy produced by bimodal microstructures provides a basis for future microstructure engineering by AM processing for other type of alloy.

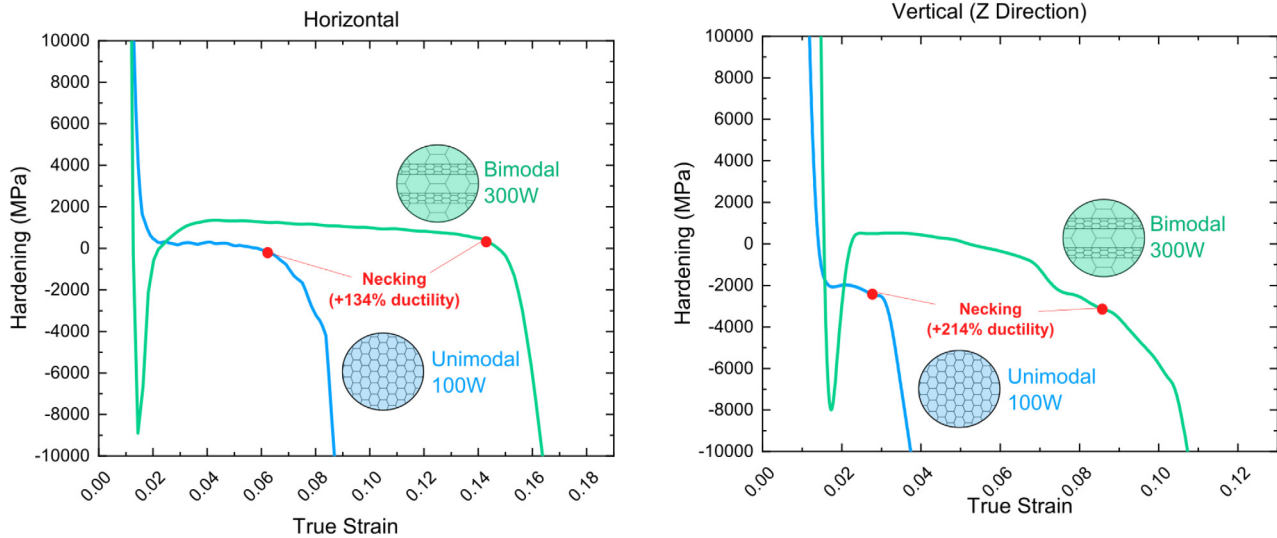


**Fig. 10.** Hardening-strain curves as a function of the sample orientation and laser power. A remarkable increase of the ductility is observed associated with the change of unimodal to bimodal microstructure.

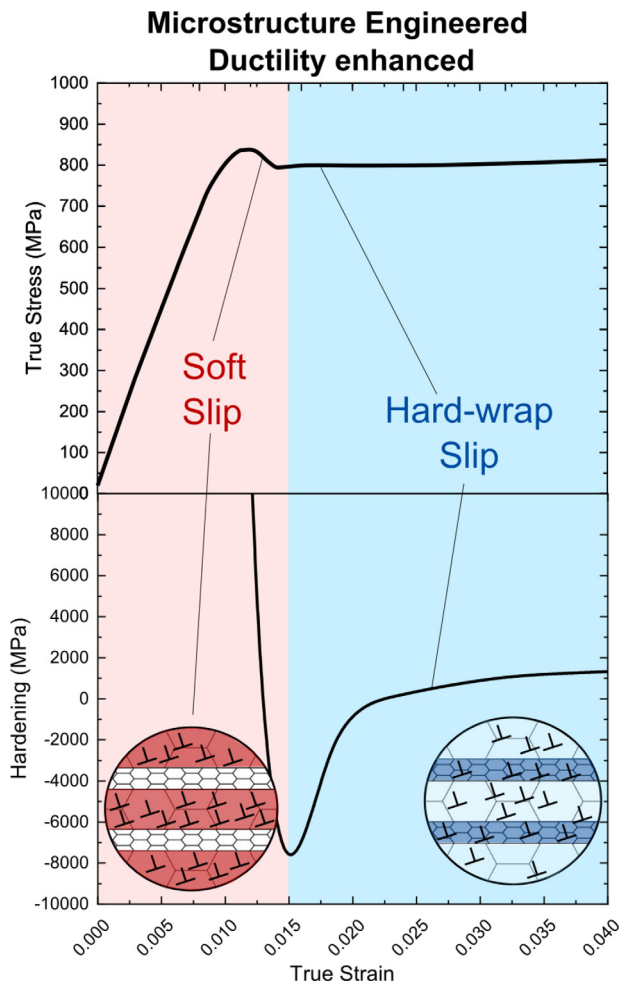


**Fig. 11.** Diagram of the plastic transition in bimodal microstructures from soft slip of large grains to hard-wrap slip.

### 3.3. On the heat-treatment induced embrittlement

In this section, the underlying processes associated with the embrittlement of the alloy after stress relief are studied. To this

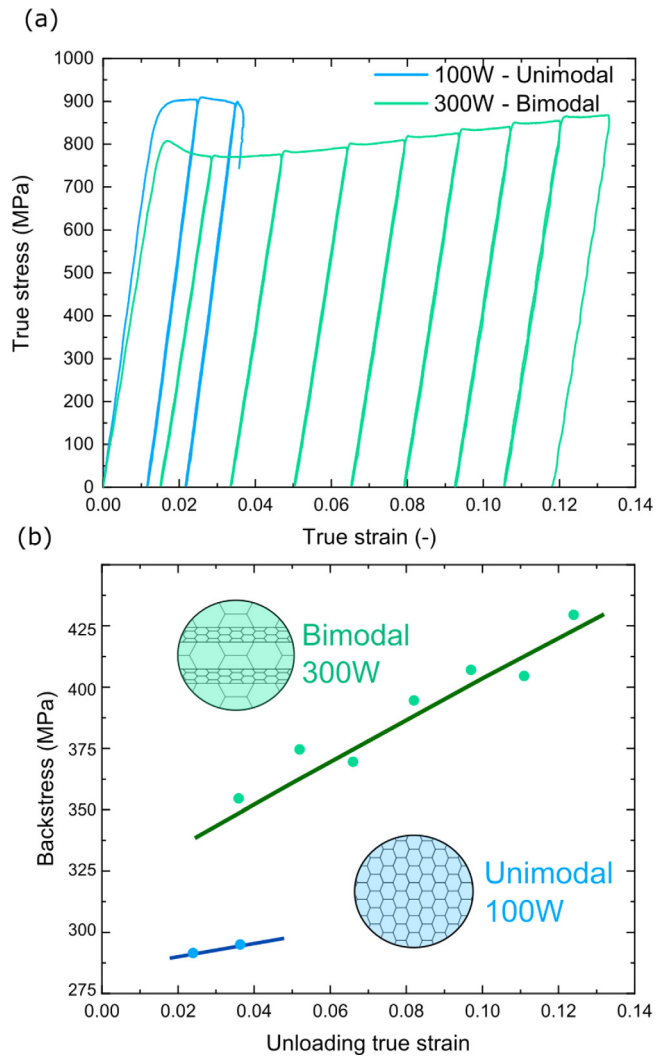


**Fig. 12.** (a) Loading-unloading-reloading stress strain curves for 100 W and 300 W samples; (b) Calculated back-stress evolution as a function of the laser power (extracted from a).

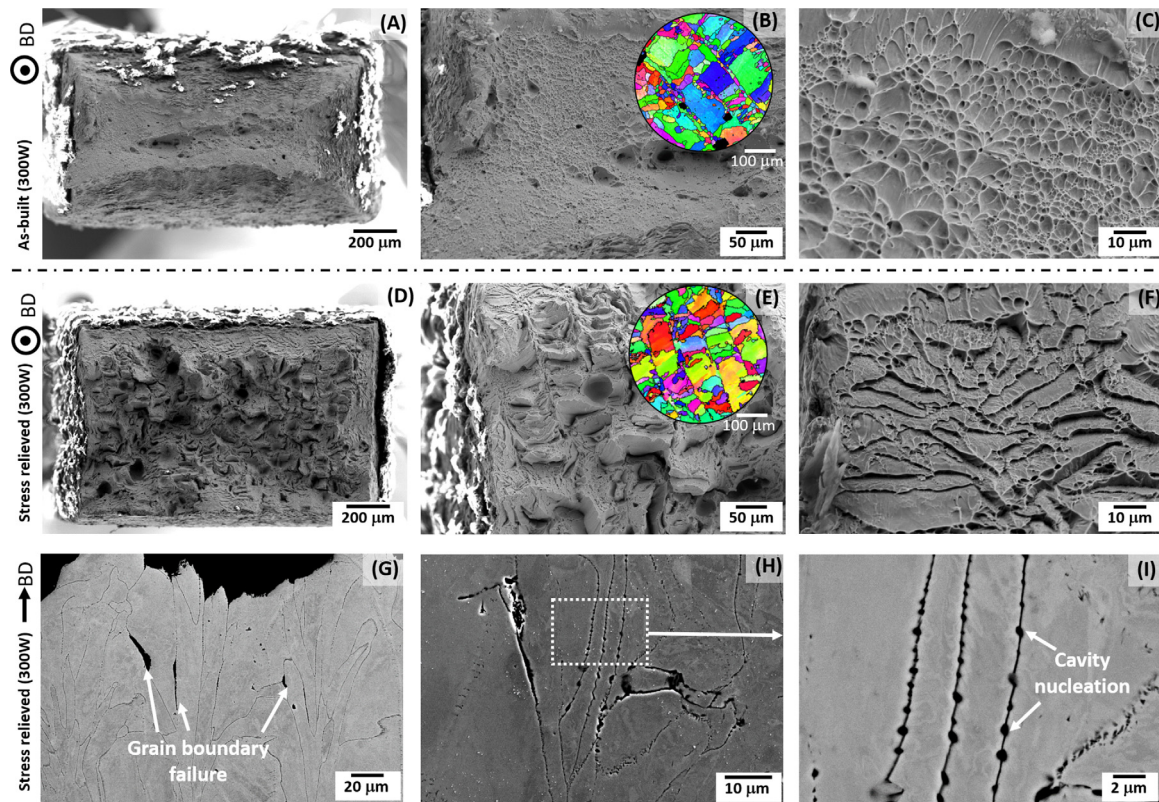


**Fig. 13.** Typical fracture surfaces observed in the as-built and stress-relieved state. (a–c) transgranular type failure observed in the as-built microstructure with dimples on the surface and (d–f) intergranular type failure observed in the stress-relieved state showing grain structures. Fractured stress-relieved microstructure viewed perpendicular to loading direction (g–i) shows grain boundary cavitation and cracking facilitated fracture.

end, a combined fracture, phase and chemical analysis of the stress-relief material is presented.

Fracture surfaces of each laser parameter in the as-built and stress-relieved conditions were characterised, see Fig. 13. The same trend was found for all three sets of parameters. Fig. 13(a) illustrates a representative fracture surface of the as-built microstructure. Higher magnifications images are shown in (b–c), where small dimples are observed. These suggest that transgranular ductile failure is predominant. For the stress-relieved samples, intergranular dominant fracture is observed. One can see clear traces of grain boundaries in Fig. 13(d–f). Furthermore, to understand the extent of the damage caused by these intergranular cracks, the surface perpendicular the loading direction was characterised – see Fig. 13(g–i). Three specific sites were imaged. One can see features that correlate to grain boundary cracking induced failure (g and h) and early stage of cavitation nucleation at boundaries (i). SEM-EDS was used to quantify the chemistry of bulk and grain boundary by analysing a line scan perpendicular to the boundary – see Fig. 15(a). The line chemistry shows an increase of Ti and O ( $\alpha$ -stabilisers) and a decrease in Nb, Ta, and Mo ( $\beta$ -stabilisers). It implies that a continuous  $\alpha$ -Ti phase layer precipitates at the grain boundaries during the stress-relief treatment, exhibiting clear a detrimental effect on the mechanical properties accounted by the grain boundary embrittlement. Based on this fracture analysis, there is a clear change in the fracture mechanisms motivated by microstructural change.

To identify changes in the microstructure, pre-tested samples were analysed using SEM microscopy before and after heat treatment. Fig. 14(a and b) shows typical microstructure of the as-built low-modulus Ti, where traces of melt-pool geometry and cellular structure can be observed. Nevertheless, the cellular structure and

**Table 2**

Laser parameters of Ti-6Al-4V tensile samples.

ID	Laser power W	Exposure time $\mu$ s	Hatch distance $\mu$ m	Point distance $\mu$ m
Ti-6Al-4V	200	50	65	56

melt-pool traces have disappeared after the stress-relief treatment, see Fig. 14(c and d). Instead, a new continuous dark phase has formed at the intergranular region missing in the as-built material.

This new phase was analysed using combined EDS and EBSD techniques, see Fig. 15. EDS line scanning shows an enrichment of Ti & O, which it suggests the phase being  $\alpha$ -Ti that is stabilised by oxygen, as identified in a similar heat treatment elsewhere [49,50]. This is further confirmed by the EBSD analysis which index  $\alpha$  brittle phase at the grain boundary. The whole embrittlement process is illustrated in Fig. 15-bottom. Small quantities of oxygen are captured in the powder from the atomisation process. During rapid solidification associated with the AM process, the oxygen is maintained as an interstitial solid solution in the  $\beta$ -phase of the alloy uniformly distributed all over the material. During the stress-relief heat treatment, oxygen gains mobility and diffuses to the grain boundaries, driven by the energy reduction associated with the distortion of the grain boundary structure. Higher concentration of localised oxygen at the grain boundary lead to an stabilisation of an oxygen rich Ti- $\alpha$  phase. The presence of oxygen rich phases in titanium alloys has been reported to be a strong embrittlement factor previously in the literature [51]. This embrittlement process should be avoided by reducing the amount of oxygen captured during the atomisation or by de-oxygenation of the powder.

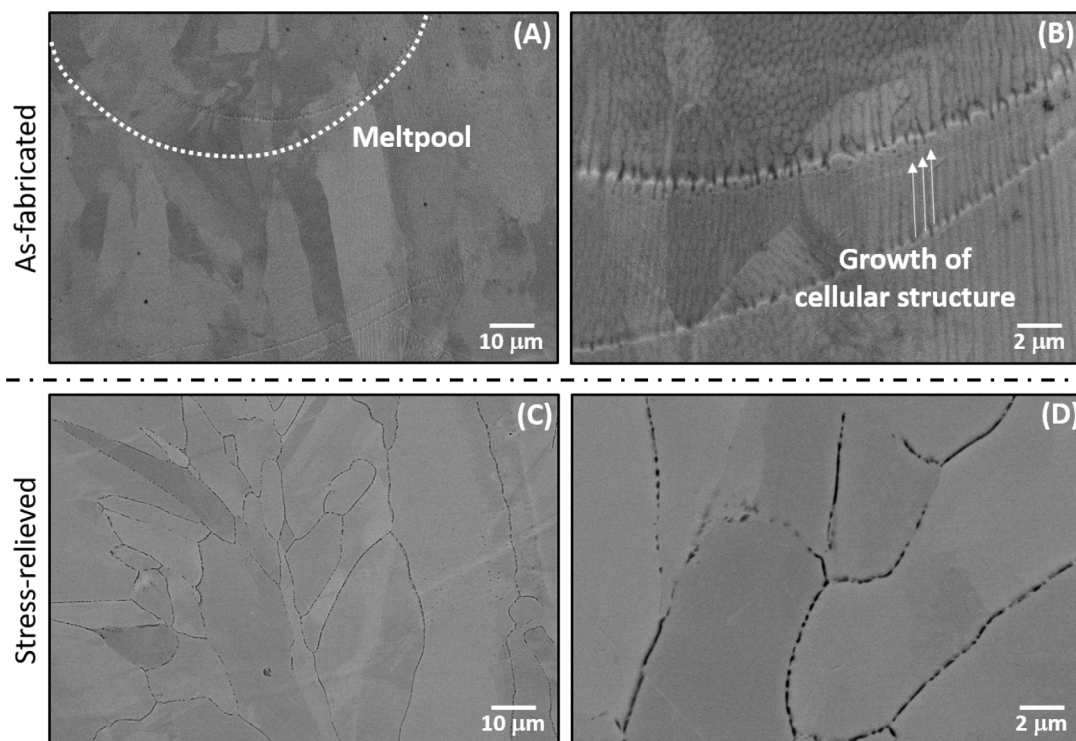


**Fig. 14.** Typical microstructure of the low modulus Ti in the as-built state (a & b) and stress-relieved state (c & d).

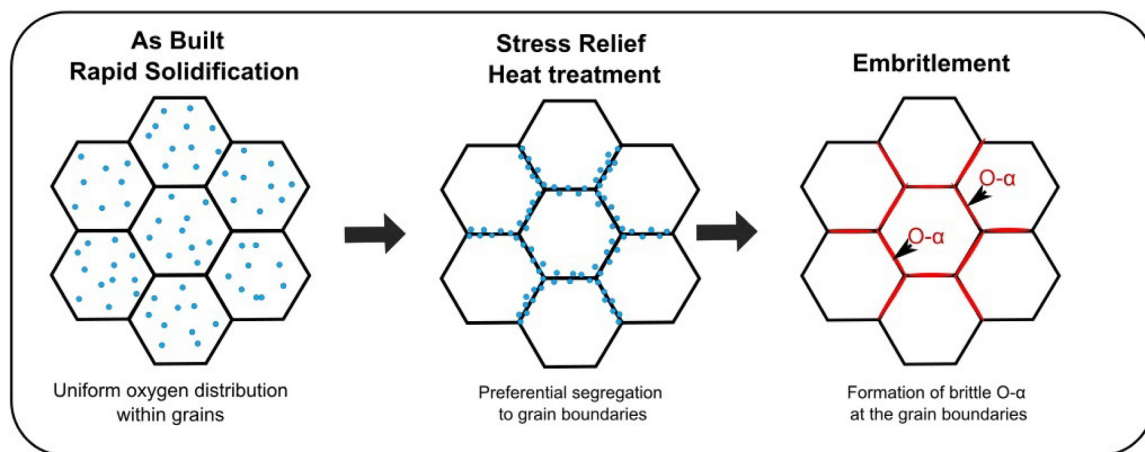
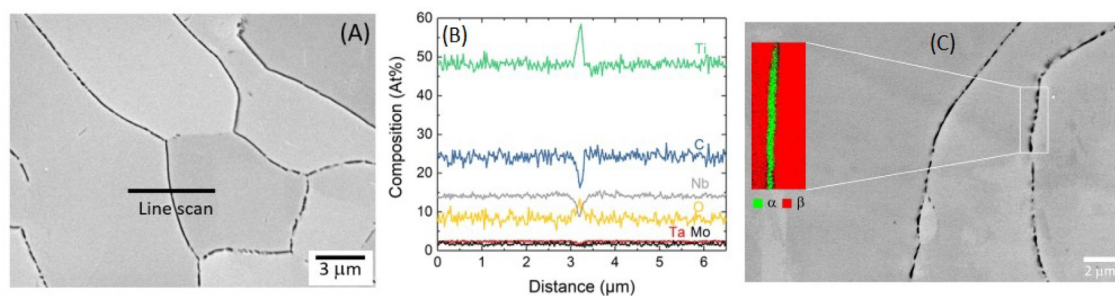


**Fig. 15.** (a) SEM-EDS line scan across two grains in the stress-relieved state; (b) Line profile in the stress-relieved microstructure showing an enrichment of Ti and O at the grain boundary; (c) High-resolution EBSD indexing of phases present at grain boundaries after heat-treatment; (bottom) Diagram of the  $\alpha$  embrittlement process observed for HT samples.

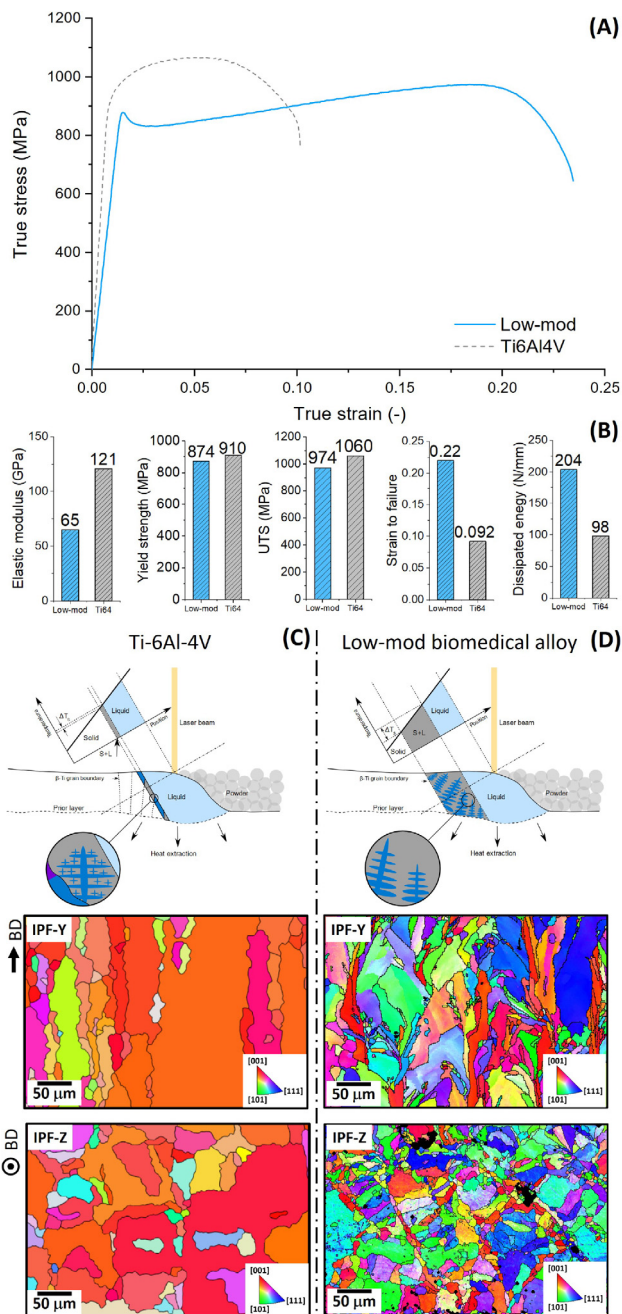


**Fig. 16.** Properties of the novel low-modulus biomedical alloy compared against SLM Ti6Al4V: (a) stress-strain curves, (b) yield strength, UTS, strain-to-failure, dissipated energy and elastic modulus. (c & d) schematic diagrams and IPF along build directions for Ti-6Al-4V and low-modulus alloy.

### 3.4. Mechanical performance comparison: new alloy vs. Ti-6Al-4V

In order to compare the behaviour of the new alloy to the current benchmark (Ti-6Al-4V), tensile bars were manufactured using standard Ti-6Al-4V parameters – these are given in Table 2.

Fig. 16 compares the stress-strain response of the low-modulus Ti alloy (as-built) to Ti-6Al-4V (stress-relieved). Fig. 16 also summarises and compares the most important mechanical values: (i) the elastic modulus, (ii) the yield strength, (iii) the ultimate tensile strength, (iv) the strain to failure, and (v) the dissipated energy. The new alloy exhibits significantly lower elastic modulus than Ti-6Al-4V, making it a superior candidate to reduce stress shielding, getting closer to the stiffness of cortical bone (10–30 GPa [52]).

Moreover, the new alloy accomplishes this with a reduced impact on yield and ultimate tensile strength – less than 10% drop. The alloy also exhibits significantly improved strain to failure and dissipated energy than Ti-6Al-4V – more than a factor of two. This increase in toughness will reduce the chances of sudden implant failure, thus increasing device safety.

Fig. 16 (b) compares the as-built microstructure of both Ti-6Al-4V alloy and the designed beta alloy. One can see that the new chemistry is able to break the planar growth observed in Ti-6Al-4V, exhibiting less elongated grains along the build direction, smaller mean grain size, and a reduction of crystallographic texture in the prior beta grain structure. This indeed proves that the growth restriction factor model is a suitable proxy to identify alloys which are more prone to create suitable microstructures during the SLM process.

## 4. Conclusions

For the first time, a biomedical  $\beta$ -titanium alloy has been designed bottom up for additive manufacture. This is also the first time that such an alloy has been atomised, processed, manufactured, and characterised via the additive method. The following specific conclusions can be drawn from this work:

1. An alloys-by-design approach has been employed which takes account of optimal additive manufacturability with only bio-compatible elements and the need for low elastic modulus achieved by promoting the metastable  $\beta$  phase. The alloy has been produced by ingot processing and atomised into powder form suitable for selective laser melting, and its properties tested extensively.
2. The desired  $\beta$  microstructure, elastic modulus and passivation is achieved by a balance of bond order, d-orbital energy levels and martensite start temperature. The additive manufacturability was predicted using solidification analysis involving solidification range, hot cracking resistance, and growth restriction factor.
3. A high-throughput parameter development campaign is carried out; relationship between melt-pool thickness and enthalpy is identified through rapid screening with single-track stability experiment. Moreover, single-track parameters are used to propose a targeted design of experiment in the form of cube build to isolate a combination of laser power, hatch distance, point distance, and exposure time parameters that result in fully dense manufacturing.
4. The relationship between optimal laser parameters – in terms of density – and mechanical properties is established. A wide tensile testing design of experiment is carried out to find the combination of laser power, exposure time and hatch distance that give rise to the lowest elastic modulus, the highest yield strength, and the largest ductility.
5. The novel alloy shows a large processing window with a wide range of laser power settings. A correlation between the geometrical features and the scan stability is determined and scaled-up for hatch parameter optimisation. It is proven that the alloy design models are adequate to allow the regime of manufacturability to be pinpointed in a right-first-time manner.
6. The relationship between the processing conditions, microstructure and mechanical properties has been rationalised using combined mechanical testing and microstructural characterisation. The peculiar bimodal distribution found at large laser powers produces a substantial increase in ductility (+100%). This is a consequence of the continuous hardening effect – boosted by the strain partitioning of the bimodal grains – retarding necking of the material.

7. Based on these insights, an optimised as-fabricated microstructure has been produced. This exhibits a desirable balance of elastic modulus, strength and ductility, despite a degree of anisotropy.
8. Stress-relief promotes the formation of a continuous  $\alpha$ -Ti layer at grain boundaries, at the expense of some ductility.

## Declaration of Competing Interest

Authors declare that they have no conflict of interest.

## Acknowledgements

The authors acknowledge funding from Innovate UK, formerly the Technology Strategy Board (TSB), under project number 104047. The authors are grateful to Alloyed Ltd for funding this research. The authors are grateful to Taniobis GmbH for producing and supplying the powder used in this study.

## Supplementary material

Supplementary material associated with this article can be found, in the online version, at doi:[10.1016/j.actamat.2022.117749](https://doi.org/10.1016/j.actamat.2022.117749).

## References

- [1] D. Raabe, B. Sander, M. Friák, D. Ma, J. Neugebauer, Theory-guided bottom-up design of  $\beta$ -titanium alloys as biomaterials based on first principles calculations: theory and experiments, *Acta Mater.* 55 (13) (2007) 4475–4487.
- [2] E. Alabort, D. Barba, R.C. Reed, Design of metallic bone by additive manufacturing, *Scr. Mater.* 164 (2019) 110–114.
- [3] S. Bahl, S. Suwas, K. Chatterjee, Comprehensive review on alloy design, processing, and performance of  $\beta$ titanium alloys as biomedical materials, *Int. Mater. Rev.* 66 (2) (2020) 1–26.
- [4] X. Zhao, M. Niinomi, M. Nakai, G. Miyamoto, T. Furuhara, Microstructures and mechanical properties of metastable Ti-30Zr-(Cr, Mo) alloys with changeable Young's modulus for spinal fixation applications, *Acta Biomater.* 7 (8) (2011) 3230–3236.
- [5] A. Biesiekierski, J. Wang, M. Abdel-Hady Gepreel, C. Wen, A new look at biomedical Ti-based shape memory alloys, *Acta Biomater.* 8 (5) (2012) 1661–1669.
- [6] D. Barba, E. Alabort, R. Reed, Synthetic bone: design by additive manufacturing, *Acta Biomater.* 97 (2019) 637–656.
- [7] M.I. Ridzwan, S. Shuib, A.Y. Hassan, A.A. Shokri, M.N. Mohammad Ibrahim, Problem of stress shielding and improvement to the hip implant designs: a review, *J. Med. Sci.* 7 (3) (2007) 460–467.
- [8] M. Niinomi, M. Nakai, Titanium-based biomaterials for preventing stress shielding between implant devices and bone, *Int. J. Biomater.* 2011 (2011).
- [9] D.R. Sumner, Long-term implant fixation and stress-shielding in total hip replacement, *J. Biomech.* 48 (5) (2015) 797–800.
- [10] S. Arabnejad, B. Johnston, M. Tanzer, D. Pasini, Fully porous 3D printed titanium femoral stem to reduce stress-shielding following total hip arthroplasty, *J. Orthop. Res.* 35 (8) (2017) 1774–1783.
- [11] Y. Yan, Y. Gong, Y. Guo, Q. Lv, C. Guo, Y. Zhuang, Y. Zhang, R. Li, X. Zhang, Mechanical strain regulates osteoblast proliferation through integrin-mediated ERK activation, *PLoS One* 7 (2012) e35709. 1–14
- [12] Y. Guo, C. Zhang, Q. Zeng, R. Li, L. Liu, Q. hao, C. Shi, X. Zhang, Y. Yan, Mechanical strain promotes osteoblast ECM formation and improves its osteoinductive potential, *BioMedical Eng. Online* 11 (80) (2012).
- [13] D. Knudson, *Fundamentals of Biomechanics*, Springer US, 1989.
- [14] M.A. Velasco, C.A. Narváez-Tovar, D.A. Garzón-Alvarado, Design, materials, and mechanobiology of biodegradable scaffolds for bone tissue engineering, *BioMed Res. Int.* 2015 (2015).
- [15] M. Long, H. Rack, Titanium alloys in total joint replacement—Amaterials science perspective, *Biomaterials* 19 (18) (1998) 1621–1639.
- [16] D. Barba, C. Alabort, Y. Tang, M. Viscasillas, R. Reed, E. Alabort, On the size and orientation effect in additive manufactured Ti-6Al-4V, *Mater. Des.* 186 (2020) 108235, doi:[10.1016/j.matdes.2019.108235](https://doi.org/10.1016/j.matdes.2019.108235).
- [17] K. Miura, N. Yamada, S. Hanada, T.-K. Jung, E. Itoi, The bone tissue compatibility of a new Ti-Nb-Sn alloy with a low Young's modulus, *Acta Biomater.* 7 (5) (2011) 2320–2326.
- [18] C.N. Elias, D.J. Fernandes, F.M. de Souza, E. dos Santos Monteiro, R.S. de Biasi, Mechanical and clinical properties of titanium and titanium-based alloys (Ti G2, Ti G4 cold worked nanostructured and Ti G5) for biomedical applications, *J. Mater. Res. Technol.* 8 (1) (2019) 1060–1069.
- [19] M.K. Han, J.Y. Kim, M.J. Hwang, H.J. Song, Y.J. Park, Effect of Nb on the microstructure, mechanical properties, corrosion behavior, and cytotoxicity of Ti-Nb alloys, *Mater.* 8 (9) (2015) 5986–6003.
- [20] L.-C. Zhang, L.-Y. Chen, A review on biomedical titanium alloys: recent progress and prospect, *Adv. Eng. Mater.* 21 (4) (2019) 1801215.
- [21] J. Markhoff, M. Krogull, C. Schulze, C. Rotsch, S. Hunger, R. Bader, Biocompatibility and inflammatory potential of titanium alloys cultivated with human osteoblasts, fibroblasts and macrophages, *Materials* 10 (1) (2017) 9–12.
- [22] Y.-J. Park, Y.-H. Song, J.-H. An, H.-J. Song, K.J. Anusavice, Cytocompatibility of pure metals and experimental binary titanium alloys for implant materials, *J. Dent.* 41 (12) (2013) 1251–1258.
- [23] B.C. Costa, C.K. Tokuhara, L.A. Rocha, R.C. Oliveira, P.N. Lisboa-Filho, J. Costa Pessoa, Vanadium ionic species from degradation of Ti-6Al-4V metallic implants: in vitro cytotoxicity and speciation evaluation, *Mater. Sci. Eng.* 96 (2019) 730–739.
- [24] J. Markhoff, M. Weinmann, C. Schulze, R. Bader, Influence of different grained powders and pellets made of Niobium and Ti-42Nb on human cell viability, *Mater. Sci. Eng.* 73 (2017) 756–766.
- [25] C. Schulze, M. Weinmann, C. Schweigel, O. Keßler, R. Bader, Mechanical properties of a newly additive manufactured implant material based on Ti-42Nb, *Materials* 11 (1) (2018) 13–16.
- [26] B. Vandenbroucke, J. Kruth, Selective laser melting of biocompatible metals for rapid manufacturing of medical parts, *Rapid Prototyp. J.* 13 (4) (2007) 196–203.
- [27] X.P. Tan, Y.J. Tan, C.S. Chow, S.B. Tor, W.Y. Yeong, Metallic powder-bed based 3D printing of cellular scaffolds for orthopaedic implants: a state-of-the-art review on manufacturing, topological design, mechanical properties and biocompatibility, *Mater. Sci. Eng.* 76 (2017) 1328–1343.
- [28] L. Hao, D. Raymont, C. Yan, A. Hussein, P. Young, Design and additive manufacturing of cellular lattice structures, *Innov. Dev. Virtual Phys. Prototyp.* (November 2014) (2011) 249–254.
- [29] L. E. Murr, S. M. Gaytan, E. Martinez, Fabricating functional Ti-alloy biomedical implants by additive manufacturing using electron beam melting, *J. Biotechnol. Biomater.* 02 (131) (2012).
- [30] S. Robinson, S. Alaie, H. Sidoti, J. Auge, L. Baskaran, K. Avilé-Fernández, S.D. Hollenberg, R.F. Sheperd, J.K. Min, S.N. Dunham, B. Mosadegh, Patient-specific design of a soft occluder for the left atrial appendage, *Nat. Biomed. Eng.* 2 (2018) 8–16.
- [31] T. DebRoy, T. Mukherjee, J. Milewski, J. Elmer, B. Ribic, J. Blecher, W. Zhang, Scientific, technological and economic issues in metal printing and their solutions, *Nat. Mater.* (2019) 181026–181032.
- [32] B. Otsuki, M. Takemoto, S. Fujibayashi, M. Neo, T. Kokubo, T. Nakamura, Pore throat size and connectivity determine bone and tissue ingrowth into porous implants: three-dimensional micro-CT based structural analyses of porous bioactive titanium implants, *Biomaterials* 27 (35) (2006) 5892–5900.
- [33] Z. Zhang, D. Jones, S. Yue, P. Lee, J. Jones, C. Sutcliffe, E. Jones, Hierarchical tailoring of strut architecture to control permeability of additive manufactured titanium implants, *Mater. Sci. Eng.* 33 (7) (2013) 4055–4062.
- [34] C. Panwisawas, Y.T. Tang, R.C. Reed, Metal 3D printing as a disruptive technology for superalloys, *Nat. Commun.* 11 (2020) 2327.
- [35] S.P. Murray, K.M. Pusch, A.T. Polonsky, C.J. Torbet, G.G. Seward, N. Zhou, S.A. Forsik, P. Nandwana, M.M. Kirka, R.R. Dehoff, W.E. Slye, T.M. Pollock, A defect-resistant Co-Ni superalloy for 3D printing, *Nat. Commun.* (2020) 4975.
- [36] T.B. Kim, S. Yue, Z. Zhang, E. Jones, J.R. Jones, P.D. Lee, Additive manufactured porous titanium structures: through-process quantification of pore and strut networks, *J. Mater. Process. Technol.* 214 (11) (2014) 2706–2715.
- [37] B. Vrancken, L. Thijs, J.-P. Kruth, J. Van Humbeeck, Microstructure and mechanical properties of a novel  $\beta$  titanium metallic composite by selective laser melting, *Acta Mater.* 68 (2014) 150–158.
- [38] E. Alabort, D. Barba, M.R. Shagiev, M.A. Murzinova, R.M. Galeyev, O.R. Valikhmetov, A.F. Aletdinov, R.C. Reed, Alloys-by-design: Application to titanium alloys for optimal superplasticity, *Acta Mater.* 178 (2019) 275–287, doi:[10.1016/j.actamat.2019.07.026](https://doi.org/10.1016/j.actamat.2019.07.026).
- [39] Yuanbo T. Tang, Chinnapat Panwisawas, Joseph N. Ghoussoub, Yilun Gong, John W.G. Clark, André A.N. Németh, D. Graham McCartney, Roger C. Reed, Alloys-by-design: Application to new superalloys for additive manufacturing, *Acta Mater.* 202 (2021) 417–436, doi:[10.1016/j.actamat.2020.09.023](https://doi.org/10.1016/j.actamat.2020.09.023).
- [40] S. Ghose, S. Babu, R.J. Van Arkel, K. Nai, P.A. Hooper, J.R. Jeffers, The influence of laser parameters and scanning strategies on the mechanical properties of a stochastic porous material, *Mater. Des.* 131 (2017) 498–508.
- [41] M. Yang, Y. Pan, F. Yuan, Y. Zhu, X. Wu, Back stress strengthening and strain hardening in gradient structure Materials Research Letters, Taylor & Francis 4 (2016) 145–151.
- [42] N. Sanaei, A. Fatemi, Defects in additive manufactured metals and their effect on fatigue performance: a state-of-the-art review, *Prog. Mater. Sci.* 117 (2021) 100724, doi:[10.1016/j.pmatsci.2020.100724](https://doi.org/10.1016/j.pmatsci.2020.100724).
- [43] V. Popovich, E. Borisov, A. Popovich, V. Sufiarov, D. Masaylo, L. Alzina, Impact of heat treatment on mechanical behaviour of inconel 718 processed with tailored microstructure by selective laser melting, *Mater. Des.* 131 (2017) 12–22, doi:[10.1016/j.matdes.2017.05.065](https://doi.org/10.1016/j.matdes.2017.05.065).
- [44] R. Ma, C. Peng, Z. Cai, R. Wang, Z. Zhou, X. Li, X. Cao, Effect of bimodal microstructure on the tensile properties of selective laser melt Al-Mg-Sc-Zr alloy, *J. Alloys Compd.* 815 (2020) 152422, doi:[10.1016/j.jallcom.2019.152422](https://doi.org/10.1016/j.jallcom.2019.152422).
- [45] H.K. Park, K. Ameyama, J. Yoo, H. Hwang, H.S. Kim, Additional hardening in harmonic structured materials by strain partitioning and back stress, *Mater. Res. Lett.* 6 (5) (2018) 261–267, doi:[10.1080/21663831.2018.1439115](https://doi.org/10.1080/21663831.2018.1439115).

- [46] J.M. Park, J. Choe, H.K. Park, S. Son, J. Jung, T.-S. Kim, J.-H. Yu, J.G. Kim, H.S. Kim, Synergetic strengthening of additively manufactured (CoCrFeMnNi)<sub>99</sub>C<sub>1</sub> high-entropy alloy by heterogeneous anisotropic microstructure, *Addit. Manuf.* 35 (2020) 101333, doi:[10.1016/j.addma.2020.101333](https://doi.org/10.1016/j.addma.2020.101333).
- [47] C. Yang, Z. Zhang, S. Li, Y. Liu, T. Sercombe, W. Hou, P. Zhang, Y. Zhu, Y. Hao, Z. Zhang, R. Yang, Simultaneous improvement in strength and plasticity of Ti-24Nb-4Zr-8Sn manufactured by selective laser melting, *Mater. Des.* 157 (2018) 52–59, doi:[10.1016/j.matdes.2018.07.036](https://doi.org/10.1016/j.matdes.2018.07.036).
- [48] J. Gibeling, W. Nix, A numerical study of long range internal stresses associated with subgrain boundaries, *Acta Metall.* 28 (12) (1980) 1743–1752, doi:[10.1016/0001-6160\(80\)90027-9](https://doi.org/10.1016/0001-6160(80)90027-9).
- [49] W. Wan, H. Liu, Y. Jiang, D. Yi, R. Yi, Q. Gao, D. Wang, Q. Yang, Microstructure characterization and property tailoring of a biomedical Ti-19Nb-1.5Mo-4Zr-8Sn alloy, *Mater. Sci. Eng.* 637 (2015) 130–138.
- [50] R. Yi, H. Liu, D. Yi, W. Wan, B. Wang, Y. Jiang, Q. Yang, D. Wang, Q. Gao, Y. Xu, Q. Tang, Precipitation hardening and microstructure evolution of the Ti-7Nb-10Mo alloy during aging, *Mater. Sci. Eng.* 63 (2016) 577–586.
- [51] M. Velasco-Castro, E. Hernández-Nava, I. Figueroa, I. Todd, R. Goodall, The effect of oxygen pickup during selective laser melting on the microstructure and mechanical properties of Ti-6Al-4V lattices, *Heliyon* 5 (12) (2019) e02813, doi:[10.1016/j.heliyon.2019.e02813](https://doi.org/10.1016/j.heliyon.2019.e02813).
- [52] M.F. Ashby, L.J. Gibson, U. Wegst, R. Olive, The mechanical properties of natural materials. I. Material property charts, *Proc. R. Soc. A* 450 (1938) (1995) 123–140.